A Deep Learning-Based Integrated Framework for Quality-Aware Undersampled Cine Cardiac MRI Reconstruction and Analysis

Inês Machado , Esther Puyol-Antón , *Member, IEEE*, Kerstin Hammernik , Gastão Cruz ,
Devran Ugurlu , Ihsane Olakorede , Ilkay Oksuz , Bram Ruijsink , Miguel Castelo-Branco ,
Alistair Young , Claudia Prieto , *Member, IEEE*, Julia Schnabel , *Fellow, IEEE*, and Andrew King

Abstract—Cine cardiac magnetic resonance (CMR) imaging is considered the gold standard for cardiac function evaluation. However, cine CMR acquisition is inherently slow and in recent decades considerable effort has been put into accelerating scan times without compromising image quality or the accuracy of derived results. In this article, we present a fully-automated, quality-controlled integrated framework for reconstruction, segmentation and downstream analysis of undersampled cine CMR data. The framework produces high quality reconstructions and segmentations, leading to undersampling factors that are optimised on a scan-by-scan basis. This results in reduced scan times and automated analysis, enabling robust and accurate estimation of functional biomarkers. To demonstrate the feasibility of the proposed approach, we perform simulations of radial k-space acquisitions using in-vivo cine CMR data from 270 subjects from the UK Biobank (with synthetic phase) and in-vivo cine CMR data from 16 healthy subjects (with real phase). The results demonstrate that the optimal undersampling factor varies for different subjects by approximately 1 to 2 seconds per slice. We show that our method can produce quality-controlled images in a mean scan time reduced from 12 to 4 seconds per slice, and that image quality is sufficient to allow clinically relevant parameters to be automatically estimated to lie within 5% mean absolute difference.

Index Terms—Cardiac MRI, deep learning, fast reconstruction, quality assessment, segmentation, UK BioBank.

I. INTRODUCTION

CARDIAC magnetic resonance (CMR) imaging is a common imaging modality for assessing cardiovascular diseases, which are the leading cause of death globally. A complete assessment of cardiac function requires images acquired over the full cardiac cycle. Although cine CMR sequences can provide these images, the acquisition process is slow. To address this, there has been significant research into accelerating acquisitions without compromising the high resolution and image quality offered by cine CMR. One promising approach is to reduce the amount of k-space data acquired. However, cine CMR reconstruction from undersampled k-space data is challenging and state-of-the-art approaches for undersampled reconstruction, such as Parallel Imaging (PI) and Compressed Sensing (CS), are computationally demanding. Recently, deep learning (DL) based reconstruction approaches have been proposed that involve the acquired k-space data and the forward model directly in the reconstruction network, achieving fast and efficient reconstruction [1], [2]. However, using current techniques the undersampling factor is fixed before acquisition to a conservative value to ensure diagnostic image quality, potentially leading to unnecessarily long scan times.

DL has also significantly impacted downstream processing of cine CMR data. Previous studies have demonstrated automated models for multi-structure segmentation, with performances matching those of human annotators [3]. Others have combined DL-based segmentation with automated analysis of volume curves to estimate a range of functional biomarkers [4]. However, the majority of these models rely on fully-sampled

Cartesian data and thus require lengthy data acquisition. An alternative approach is segmentation estimation directly from undersampled k-space data [5], but bypassing the reconstructed images in this way raises questions of interpretability and clinician trust, and presupposes that the images themselves are not needed for clinical purposes.

Traditionally, cine CMR acquisition, reconstruction and analysis have been considered as independent steps, despite the obvious inter-dependence between high-quality image reconstruction and high accuracy in downstream tasks, such as segmentation and quantification [6]. Some preliminary work has combined the reconstruction and segmentation processes in a joint DL-based framework [7]. However, this was aimed at detecting and correcting for imaging artefacts, not at speeding up the acquisition. Furthermore, quality control (QC) of downstream analysis is an essential component of a clinically-applicable CMR pipeline. Ideally, this QC should be performed whilst the patient is still in the scanner, so that a new scan could be acquired if the original scan was not of sufficient quality. Existing work has not addressed the incorporation of QC into an integrated reconstruction, segmentation and analysis framework.

We hypothesise that the use of a pre-defined undersampling factor for a cine CMR acquisition is not optimal in terms of image quality and/or scan efficiency. Rather, the optimal undersampling factor should be determined using the data acquired during scanning. To test this hypothesis, in this article we propose a DL-based framework that integrates cine CMR acquisition, reconstruction and downstream analysis with QC. The framework aims to ensure that sufficient data are acquired to produce images of diagnostic quality and reliable estimates of cardiac functional parameters but that scan efficiency is not compromised by acquiring further data once sufficient quality has been achieved. Our ultimate aim is to develop an active acquisition framework in which scanning is stopped in real-time once QC checks are passed. This article presents a proof-of-concept of this idea based on simulations using retrospectively undersampled k-space data. The framework we propose aims at fast analysis of undersampled cine CMR data, not only optimising typically lengthy acquisition times on a scan-by-scan basis, but also enabling automated functional quantification from the reconstructed images.

The remainder of this article is organised as follows: Section II presents a literature review and our novel contributions in this context. Section III describes the clinical datasets used. Section IV describes our proposed framework for QC-driven reconstruction and analysis of undersampled cine CMR k-space data, including descriptions of each section of the framework. Experiments and Results are presented in Sections V and VI, respectively, while Section VII discusses the findings of this article in the context of the literature and suggests potential directions for future work.

II. RELATED WORK

A. Acquisition and Reconstruction

Considerable effort has been devoted to accelerate the reconstruction of cine CMR from undersampled k-space data including PI [8] and CS [9]. CS approaches work by exploiting redundancy or assumptions about the underlying data to resolve the aliasing caused by sub-Nyquist sampling. CS is computationally demanding, motivating recent research into learning the reconstruction mapping from k-space data to reconstructed images via convolutional neural networks (CNNs) [10], [11]. It has been shown that CNNs outperform sparsity-based methods with respect to both reconstruction quality and speed [12]. DL solutions for CMR reconstruction in general can be classified as those that mimic the optimization process of iterative reconstruction approaches by unrolling the process into several stages, such as [1] and [2], and those that pursue reconstruction as a black-box model, such as [13] and [14]. For instance, the method proposed in [1] describes a deep neural network trained to reconstruct cine sequences of CMR images. This results in an iterative procedure consisting of a cascade of two structures, a Deep Network (DN) and a Data Consistency (DC) unit. More recently, DL approaches have been proposed by exploiting spatio-temporal redundancy via recurrent CNNs [11]. For example, Küstner et al. proposed the CINENet network for 3D+time cine CMR reconstruction and showed that it outperforms iterative reconstruction in terms of visual image quality and contrast [10].

B. Segmentation and Quantification

Image segmentation is an important downstream task for many cardiovascular clinical applications. Segmentation enables the quantification of parameters that describe cardiac morphology, such as left ventricle (LV) and right ventricle (RV) end-diastolic (ED) and end-systolic (ES) volumes, or cardiac function, e.g. myocardial wall thickening and ejection fraction (EF). A large body of research has been dedicated to developing automated cine CMR segmentation methods [15]. Many such methods are based on the U-Net architecture [16]. For instance, a basic CNN architecture with 9 convolutional layers and a single up-sampling layer was used to segment short-axis (SAX) cine CMR images [17]. Another example is a fully convolutional approach with a simpler up-sampling path that was successfully applied for pixel-wise segmentation of 4-chamber, 2-chamber and SAX cine CMR images in less than 1 min [3]. More recently, the nnU-Net framework [18] has shown state-of-the-art performance for automatic segmentation of both ventricles and the myocardium from cine CMR [19]. nnU-net was the top-performing model in the Automated Cardiac Diagnosis Challenge (ACDC) CMR segmentation challenge [20]. Once accurate cine CMR segmentations have been produced, morphological and functional parameters can be calculated from the segmentations. Frameworks have been proposed for estimating LV and RV volumes and EF [21], with others going further by estimating parameters from the atria and aorta [22] as well as a wider range of systolic and diastolic functional parameters [4]. Some of these frameworks [4], [21] also incorporate QC checks to enable their use in clinical imaging and retrospective population studies.

C. Quality Control

In the medical imaging domain, quality assessment is an important topic of research in the fields of image

acquisition, reconstruction and segmentation. In acquisition and reconstruction, motion during the CMR scanning process is a major source of image degradation [23]. This can lead to artefacts such as blurring, ghosting, and breath-hold slice misalignment. It is important to be able to automatically detect when a reconstruction method fails, so as to avoid inclusion of wrong measurements into subsequent analyses and potentially incorrect conclusions. Work on QC in general MR imaging includes Küstner et al., who proposed to extract a set of features and trained a deep neural network for artefact detection [24]. Previous work on QC in cine CMR imaging includes Zhang et al. [25], who proposed a method to identify missing apical and basal slices. More recently, Oksuz et al. [26] used a curriculum learning strategy exploiting different levels of k-space corruption to detect cardiac motion artefacts. This work was extended in [7] to both detect and correct for the motion artefacts. In clinical applications, using erroneous segmentations of medical images can have dramatic consequences. Recently, methods have been proposed to detect segmentation failures in large-scale CMR imaging studies for removal from subsequent analyses. Using the approach of Reverse Classification Accuracy (RCA), Robinson et al. [27] predicted cine CMR segmentation metrics to identify failed segmentations, achieving good agreement between predicted metrics and visual QC scores. Galati et al. [28] proposed a convolutional autoencoder to quantify segmentation quality at inference time, without a ground truth (GT). More recently, Fournel et al. [29] proposed a new CNN-based segmentation QC approach by training a DL classifier on CMR images and derived segmentations to predict quality.

D. Contributions

There are four major contributions of this work:
- We propose a DL-based and QC-driven integrated framework which can automatically reconstruct and segment undersampled cine SAX CMR images at all time points across the cardiac cycle and, from these, derive functional biomarkers.
- The framework includes robust pre- and post-analysis QC mechanisms to detect high-quality image reconstructions and segmentations.
- Importantly, the framework allows the potential for acquisition to be stopped as soon as acquired data are sufficient to produce high quality reconstructions and segmentations. This enables the future implementation of an active acquisition scheme in which the undersampling factor is optimised on a scan-by-scan basis.
- We show that quality-controlled cine CMR images can be reconstructed from a scan time reduced from 12 to 4 seconds per slice, and that image quality is sufficient to allow for clinically relevant parameters to be automatically estimated to within 5% mean absolute error.

This article builds upon our previous work on cine CMR reconstruction and analysis [30]. Here, we extend this preliminary work in two main ways. First, we include a DL-based segmentation QC step that enables our framework to be run in real-time. This is an important requirement for our ultimate aim of developing an active acquisition process in which the quality of reconstructed images and derived segmentations can be used to control the k-space profile acquisition process, resulting in faster acquisitions. Second, for our evaluation, we improve the realism of the simulations by making use of in-vivo acquisitions with real phase information, in addition to the experiments with simulated phase we previously performed.

III. MATERIALS

A. UK Biobank Cine CMR Magnitude Imaging Data

The reconstruction and segmentation models were trained using a subset of 4,875 in-vivo cine SAX CMR scans acquired from healthy subjects from the UK Biobank. The QC models were trained using an additional set of 100 cases from the UK Biobank. The UK Biobank cine CMR scans were all acquired using a 1.5 Tesla MRI scanner (MAGNETOM Aera, Siemens Healthcare, Erlangen, Germany). The SAX image acquisition typically consists of 10 image slices with a field of view of 380×252 mm and a slice thickness of 8 mm, covering both ventricles from the base to the apex. The in-plane image resolution is 1.8×1.8 mm^2, the slice gap is 2 mm, with a repetition time (TR) of 2.6 ms and an echo time (TE) of 1.10 ms. Each cardiac cycle consists of 50 time frames. The average (min - max) heart rate for these cases is 65.4 (56.3–99.7) bpm. More details of the image acquisition protocol can be found in [31]. To train the segmentation model, pixel-wise segmentations of three structures (LV, RV, and myocardium) for both ED and ES frames were manually performed to act as GT segmentations. The segmentations were performed by a group of eight observers and each subject was annotated only once by one observer. Visual QC was performed on a subset of the data to ensure acceptable inter-observer agreement. The segmentation model was evaluated using 600 different subjects (with GT segmentations of the three structures) from the UK Biobank for intra-domain testing and two other datasets for cross-domain testing: the ACDC dataset (100 subjects, 1 site, 2 scanners) and the British Society of Cardiovascular Magnetic Resonance Aortic Stenosis (BSCMR-AS) dataset (599 subjects, 6 sites, 9 scanners).

In addition, an extra cohort of healthy (n = 200) and cardiomyopathy (n = 70) cases from the UK Biobank was used to evaluate the complete framework. These were not used for training/testing/validating any component of the framework.

B. Cine CMR Complex Imaging Data

In-vivo cine CMR k-space data from 16 healthy subjects were acquired using a tiny golden angle radial bSSFP sequence with angular step of $23°$ on a 1.5 Tesla MRI scanner (Ingenia, Philips, Best, The Netherlands). Further acquisition parameters are: TR = 2.3 ms, TE = 1.1 ms, in-plane resolution = 2 mm $\times$ 2 mm, slice thickness = 8 mm, flip angle = $60°$ and number of channels = 28. Retrospective ECG-triggering was used to reconstruct 25 cardiac phases in a segmented fashion. The total scan time was 20 heartbeats on average. Ethical approval was obtained and all subjects provided informed consent.
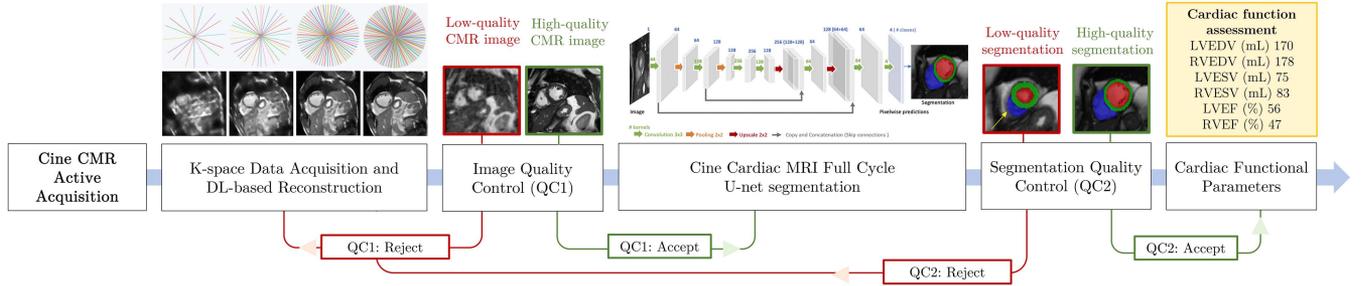
Fig. 1. Overview of the image analysis pipeline for fully-automated cine CMR undersampled reconstruction and analysis including comprehensive QC algorithms to detect erroneous output. As k-space profiles are acquired, images are continually reconstructed using a Deep Cascade of Convolutional Neural Networks (DCCNN) and passed through QC checks: QC1 to detect high-quality reconstructions and QC2 to detect high-quality segmentations. The simulated acquisition terminates when the reconstructed images pass all QC checks.
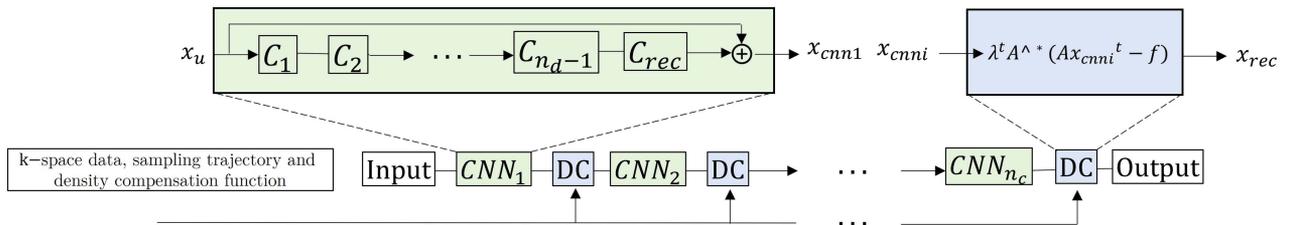

Fig. 2. Cascade of CNNs. $x_u \in \mathbb{C}^N$ represent a sequence of 2D complex-valued MR images stacked as a column vector, where $N = N_x \, N_y \, N_t$. To obtain a reconstruction, we feed the undersampled k-space data, sampling trajectory and density compensation function to the network. CNN and DC denotes the convolutional neural network and the data consistency layer, respectively. The number of convolutional layers C_i within each network and the depth of cascade is denoted by n_d and n_c respectively. The final layer of the CNN module is a convolution layer C_{rec} which projects the extracted representation back to the image domain. The data consistency layers follow a gradient descent scheme, where A^* is the adjoint linear sampling operator, f is the given undersampled k-space data and t is the iteration number, according to [2]. During the training procedure, the filter kernels, activation functions and data term weights λ^t are learned.

IV. METHODS

In this section, we describe the integrated framework for quality-controlled cine CMR image acquisition, reconstruction and downstream analysis. We provide details of the specific models used for the reconstruction of 2D+time cine SAX CMR from undersampled k-space data (Section IV-A), image QC to detect high-quality reconstructions (Section IV-B), bi-ventricular segmentation (Section IV-C), a QC step to detect high-quality segmentations (Section IV-D) and automated calculation of cardiac functional parameters (Section IV-E). The illustration of the pipeline can be seen in Fig. 1.

A. Reconstruction

As k-space profiles are acquired during simulated acquisition, images are continually reconstructed using the Deep Cascade of Convolutional Neural Networks (DCCNN) method [1], a CNN-based framework for reconstructing MR images from undersampled data to accelerate the data acquisition process. DCCNN features alternating data consistency layers and regularisation layers within an unrolled end-to-end framework. Undersampled k-space data, along with the sampling trajectory and density compensation function, are provided as input to this unrolled model for DL reconstruction, and high-quality CMR images are obtained as an output in an end-to-end fashion. The regularisation layers of this network were implemented

as a 5-layer CNN according to [1], and the data consistency layers follow a gradient descent scheme according to [2]. The Cartesian operator was extended to a non-Cartesian version using the GPU-nuFFT package [32]. The reconstruction model was trained using a subset of 4,875 cine CMR scans acquired from healthy subjects from the UK Biobank (3,975 cases were used for training, 300 for validation, and 600 for testing the model). More details of the image reconstruction method can be found in [2]. The network architecture for the CNN is illustrated in Fig. 2.

B. Image Quality-Control Network

The first QC step (QC1) was framed as a binary classification problem and addressed using a ResNet classification network [33]. We chose a residual network because it can make the training process faster and it achieves state-of-the-art performance. For training the ResNet, the UK Biobank data from 100 healthy subjects were used to simulate cine series based on undersampled radial k-space trajectories containing increasing numbers of profiles corresponding to scan times between 1 to 30 seconds, in steps of 1 second. The k-space data were reconstructed using the DCCNN reconstruction model. Slice-level binary image quality labels (analyzable/non-analyzable) were generated by an expert cardiologist with more than 10 years of experience from 30,000 2D images (100 subjects *
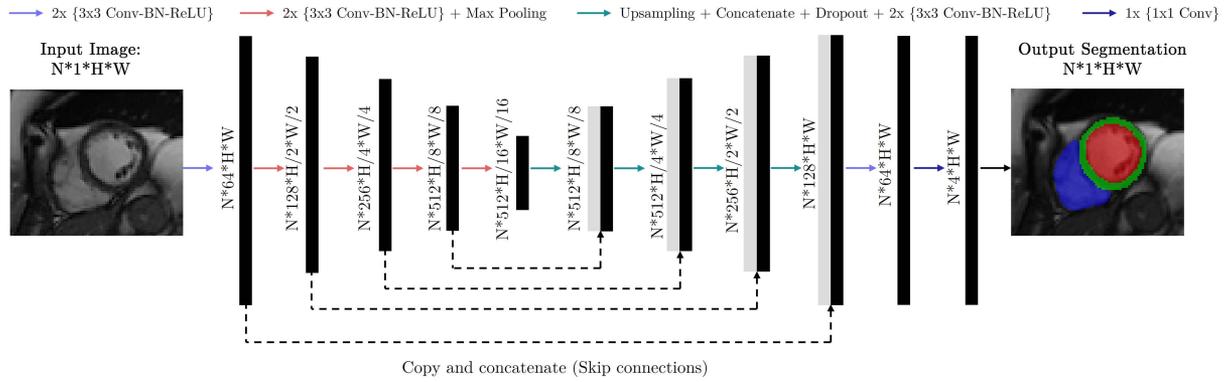
Fig. 3. U-net architecture used for segmentation of 2D+time CMR sequences. The U-Net takes a batch size of N 2D CMR images as input at each iteration, learning multi-scale features through a series of convolutional layers and max-pooling operations. These features are then combined through upsampling and convolutional layers from coarse to fine scales, generating pixel-wise predictions for the four classes (background, LV, RV and myocardium) on each slice. Conv: Convolutional layer; BN: Batch normalization; ReLU: Rectified linear unit.

10 slices * 2 time frames * 15 undersampling factors) at different levels of undersampling. Visual QC was performed on 30% (corresponding to 9,000 2D images) of the data to ensure acceptable inter-observer agreement. Images were considered to be high-quality if they were acquired at the correct slice location, were artefact-free and had good image contrast throughout the cardiac cycle. Due to the imbalance in the labels, we used the precision-recall metric to evaluate classifier output quality. Prior to training, all images were cropped to a standard size of 192×192 pixels and 80% were used for training, 10% for validation, and 10% for testing the network. The ResNet was trained for 200 epochs with a binary cross entropy loss function. During training, data augmentation was performed on-the-fly including rotation, shifts and image intensity transformations. The probability of augmentation for each of the parameters was 50%. The training/validation/testing images for QC1 were randomly selected from the UK Biobank dataset and were not used for training or evaluating the reconstruction/analysis framework.

C. Full Cycle Image Segmentation

We used a U-net based architecture for automatic segmentation of the LV blood pool, LV myocardium and RV blood pool from all SAX slices and all frames throughout the cardiac cycle. Fig. 3 shows the U-net architecture used for segmentation of the cine sequences. The subset of the UK Biobank dataset with GT annotations was split into 3,975, 300 and 600 subjects for training, validation and testing respectively. All images were resampled to 1.25×1.25 mm. The training dataset was augmented in order to cover a wide range of geometrical variations in terms of the heart pose and size. During training, the dropout rate for each layer was set to be 0.2. In every iteration, cross entropy loss was calculated to optimize the network parameters through back-propagation. Specifically, the stochastic gradient descent (SGD) method was used during the optimization, with an initial learning rate of 0.001. The learning rate was decreased by a factor of 0.5 every 50 epochs. More details of the image segmentation method can be found in [34].

D. Segmentation Quality-Control Network

The second QC step (QC2) was also framed as a binary classification problem and addressed using a ResNet classification network [33], which took an image-segmentation pair as input, similar to [29]. To define the binary labels, we first calculate the Dice Similarity Coefficient (DSC) per-class (LV and RV blood pool and LV myocardium) between predicted segmentations and the manually-labelled segmentations (described in Equation 4). A good quality pair was assumed to have a mean DSC for all classes above 0.7 and the slice-level binary labels were defined accordingly. To train and evaluate QC2, we used a subset of 100 subjects from the UK Biobank. This resulted in a total of 30,000 samples (100 subjects * 10 slices * 2 time frames * 15 undersampling factors). Due to the imbalance in the DSC scores, we chose to sample the DSC distribution using the following bins: [0, 0.2], [0.2, 0.3], [0.3, 0.4], [0.4, 0.5], [0.5, 0.6], and [0.7, 1]. We then took a fixed number of segmentations from each bin, equal to the minimum number of counts-per-bin across the distribution as in [29]. Our final dataset comprised 23,520 samples. We split the data at the subject level 80:10:10 giving 18,816 training samples and 2,352 samples each for validation and testing. The ResNet was trained for 200 epochs with a binary cross entropy loss function and a precision-recall metric to evaluate classifier output quality. During training, data augmentation was performed on-the-fly including rotation, shifts and image intensity transformations. The probability of augmentation for each of the parameters was 50%. The training/validation/testing images for QC2 were randomly selected from the UK Biobank dataset and were not used for training or evaluating any other parts of the reconstruction/analysis framework.

E. Clinical Functional Parameters

A range of functional biomarkers were derived from the image segmentations. We calculated the left ventricle end-diastolic volume (LVEDV), left ventricle end-systolic volume (LVESV), left ventricle ejection fraction (LVEF), right ventricle end-diastolic volume (RVEDV), right ventricle end-systolic volume (RVESV) and right ventricle ejection fraction (RVEF). The volumes were

calculated by multiplying the number of voxels across all slices by the voxel volume for each of the LV/RV classes. The maximum volume over the cardiac cycle was used for (LV/RV)EDV and the minimum for (LV/RV)ESV. EF (for both LV and RV) was calculated as (EDV-ESV)/EDV. Two measures were used to examine differences, namely the absolute and relative differences. The absolute difference is the actual difference between the predicted value and the reference value. The relative difference describes the size of the absolute difference as a fraction of the reference value.

F. Implementation Details

All experiments were performed on a single desktop computer equipped with a quad-core 3.5 GHz CPU, 16 GB RAM and an NVIDIA GTX 1080 Ti GPU. The Pytorch framework was used for implementation.

V. Experiments

Section V-A describes the metrics used to validate image and segmentation quality. We evaluated our framework using two types of experiment. In Experiment 1, we used reconstructed cine CMR magnitude images from the UK Biobank (see Section III-A) in order to generate synthetic complex-valued k-space data by simulating phase and a golden-angle radial acquisition process, as described in Sections V-B and V-D, respectively. In Experiment II, we used cine CMR complex images (see Section III-B) generated as sensitivity-weighted coil-combination with original magnitude and phase information and simulated a golden-angle radial acquisition process, as described in Sections V-C and V-D, respectively. Section V-E describes the reconstruction methods used for comparison.

A. Evaluation Metrics

Image quality was evaluated with Mean Absolute Error (MAE), Structural Similarity Index (SSIM) and Peak Signal to Noise Ratio (PSNR), defined in Equations (1), (2) and (3), respectively.

$$\text{MAE} = \frac{1}{N_p} \sum_{p=1}^{N_p} |(I_x(p) - I_y(p))| \tag{1}$$

where p corresponds to each pixel in a total of N_p pixels in reference and predicted images I_x and I_y.

$$\text{SSIM}(p) = \frac{(2\mu_x\mu_y + c_1)(2\sigma_{xy} + c_2)}{(\mu_x^2 + \mu_y^2 + c_1)(\sigma_x^2 + \sigma_y^2 + c_2)} \tag{2}$$

where (μ_x, σ_x) and (μ_y, σ_y) correspond to the average intensities and variance values for regions x and y, respectively. σ_{xy} is the covariance of regions x and y and c_1 and c_2 are constant values for stabilising the denominator.

$$\text{PSNR} = 20 \log_{10}(\max(I))$$
$$- 10 \log_{10} \left(\frac{1}{N_p} \sum_{p=1}^{N_p} (I_x(p) - I_y(p))^2 \right) \tag{3}$$

where $\max(I)$ corresponds to the maximum intensity value in the reference image. To evaluate the quality of segmentations, the DSC overlap measure was computed. DSC is defined between two regions A and B by Equation (4).

$$DSC(A, B) = \frac{2\|A \cap B\|}{\|A\| \cup \|B\|}. \tag{4}$$

DSC is a value between 0 and 1, with 0 denoting no overlap and 1 denoting perfect agreement. The higher the DSC value, the better the agreement.

B. Experiment I: Retrospective Undersampling From UK Biobank Data With Simulated Phase

To train the reconstruction and QC models, the UK Biobank data were used to simulate cine CMR images based on undersampled radial k-space trajectories with a golden-angle step (TR = 2.6 ms) containing increasing numbers of profiles corresponding to scan times between 1 to 30 seconds, in steps of 1 second. Phase information is an important source of data in cine CMR image reconstruction. However, the UK Biobank dataset contains only the reconstructed magnitude images. In this experiment, we therefore use reconstructed cine CMR images from the UK Biobank to produce fully-sampled complex-valued k-space data with synthetic phase information. More details on the dataset used in this experiment can be found in Section III-A. To generate the synthetic phase, we used an approach similar to [35]. White Gaussian noise was added to the original images and then a Fourier Transform was applied to generate k-space data. A low pass filter was then applied to the k-space data followed by an inverse Fourier transform to produce the complex image data. We used these data to simulate an acquisition process by using a radial golden-angle sampling pattern to produce undersampled k-space with varying undersampling factors as described in Section V-D. The golden angle sampling used in this work takes into account the k-space sampling pattern and image artefacts caused by applying golden radial acquisition to segmented ECG-gated cardiac MRI applications. The functional metrics estimated from the undersampled reconstructed images that passed the QC checks with the lowest scan time during simulated acquisition were compared to those derived from the GT segmentations of the fully-sampled images.

C. Experiment II: Retrospective Undersampling From Complex Coil-Combined Fully-Sampled Data

In this experiment, we used tiny golden-angle radially-acquired cine CMR fully-sampled complex-valued k-space data from 16 healthy subjects. Note that these data contain original phase and magnitude information. More details on the dataset used in this experiment can be found in Section III-B. We used these data to simulate an acquisition process by using a radial golden-angle sampling pattern to produce undersampled k-space with varying undersampling degrees, as described in Section V-D. During our experiments, we used a single slice per breath hold and we therefore treated each slice independently. The functional metrics estimated from the undersampled reconstructed images that passed the QC checks with the lowest

		nuFFT		XD-GRASP		DCCNN	
		Healthy	Disease	Healthy	Disease	Healthy	Disease
Exp. I	MAE	0.03 ± 0.03	0.05 ± 0.04	0.03 ± 0.02	0.04 ± 0.02	0.02 ± 0.04	0.04 ± 0.03
	PSNR	30.55 ± 0.06	29.82 ± 0.06	30.94 ± 0.07	29.96 ± 0.07	31.10 ± 0.06	30.09 ± 0.07
	SSIM	0.87 ± 0.04	0.87 ± 0.05	0.90 ± 0.04	0.89 ± 0.04	0.91 ± 0.03	0.90 ± 0.04
Exp. II	MAE	0.04 ± 0.03	N/A	0.03 ± 0.05	N/A	0.03 ± 0.04	N/A
	PSNR	30.82 ± 0.05	N/A	32.01 ± 0.05	N/A	32.07 ± 0.06	N/A
	SSIM	0.89 ± 0.04	N/A	0.89 ± 0.03	N/A	0.91 ± 0.03	N/A

The mean and standard deviation are reported. In experiment II, all cases correspond to healthy subjects. MAE: Mean absolute error. SSIM: Structural similarity index. PSNR: Peak signal to noise ratio.

scan time during simulated acquisition were compared to those derived from the GT segmentations of the fully-sampled images.

D. Simulation of Radial Acquisition Pattern

We simulated an acquisition process by using a radial golden-angle sampling pattern to produce undersampled k-space data from simulated phase (Experiment I) and original phase (Experiment II) fully-sampled reconstructed images. These data contain increasing numbers of profiles corresponding to scan times between 1 to 30 seconds, in steps of 1 second. To simulate the undersampled radial k-space acquisition, the images were organized into 3D matrices. The resulting matrix was Fourier transformed along the spatial domains and each $(k_x\text{-}k_y)$ space was masked by a radial pattern with a TR of 2.6 ms. For each sample, the number of projections per frame (t) was equal to $P \in \{7, 15, 23, 30, 38, 46, 53, 61, 69, 77, 84, 92, 100, 107, 115, 123, 130, 138, 146, 153, 161, 169, 176, 184, 192, 200, 207, 215, 223, 230\}$ corresponding to thirty different sampling rates. Accordingly, the corresponding acceleration factors R with respect to the radial fully-sampled data were $\{41.96, 19.58, 12.77, 9.79, 7.73, 6.39, 5.54, 4.82, 4.26, 3.81, 3.5, 3.19, 2.94, 2.74, 2.55, 2.39, 2.26, 2.13, 2.01, 1.92, 1.83, 1.74, 1.67, 1.60, 1.53, 1.47, 1.42, 1.37, 1.32, 1.28\}$. The angle increment between projections within one frame was set to the golden angle [36]. The obtained series was transformed back to image space representing reconstructions of undersampled k-spaces, as shown in Fig. 4.

E. Reconstruction Methods

As well as our proposed DCCNN reconstruction approach described in Section IV-A, we performed a comparative evaluation with state-of-the-art reconstruction methods. We used the non-uniform Fast Fourier Transform (nuFFT) [37] and, in the compressed-sensing domain, we used an in-house implementation of the Extra-dimensional golden-angle radial sparse parallel (XD-GRASP) reconstruction method following the description in [38].

VI. RESULTS

We now present results that illustrate the ability of our integrated framework to produce high-quality image reconstructions and segmentations (Sections VI-A and VI-B, respectively)
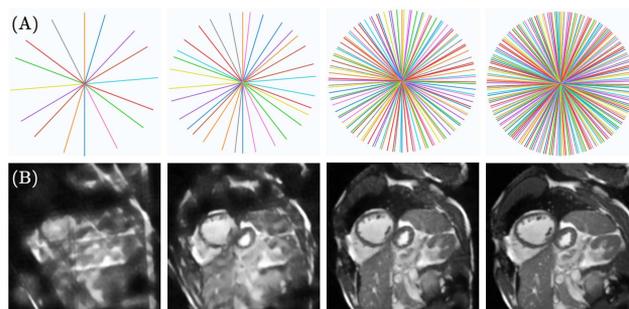

Fig. 4. Simulation of radially undersampled data from fully-sampled Cartesian data. Pseudo-radial patterns (A) were used to mask the Cartesian grid with a different number of projections as described in Section V-D. (B) shows the result of applying the simulated undersampling to the fully-sampled data. After each acquisition of radial profiles, the undersampled k-space data were used as input to our framework.

and accurate estimates of cardiac functional parameters (Section VI-C). Section VI-D shows differences in terms of scan time and acceleration factors between the fully-sampled acquisition and our integrated framework. A qualitative assessment of the framework was also performed and results can be found in Section VI-E.

A. Image Quality Analysis

Image quality was evaluated with MAE, PSNR and SSIM and calculated between the fully-sampled image and the undersampled image that passed QC1 with the lowest scan time during simulated acquisition. Table I shows these metrics for Experiments I and II. We show these results for the three reconstruction methods and also separately for healthy subjects and cardiomyopathy patients. Results are similar between healthy and cardiomyopathy patients and between the three reconstruction methods and comparable with those reported in [7] for cine CMR image quality showing the ability of the QC check to detect high-quality reconstructions across different reconstruction algorithms and healthy/disease cases. The QC1 ResNet balanced accuracy (BACC), sensitivity (SEN) and specificity (SPE) on the testing set were equal to 92.5%, 90% and 95%, respectively, for the nuFFT, 94%, 91% and 97%, respectively, for the XD-GRASP and 93.5%, 91% and 96%, respectively, for the DCCNN. Fig. 5 illustrates cine CMR image reconstructions, segmentations and
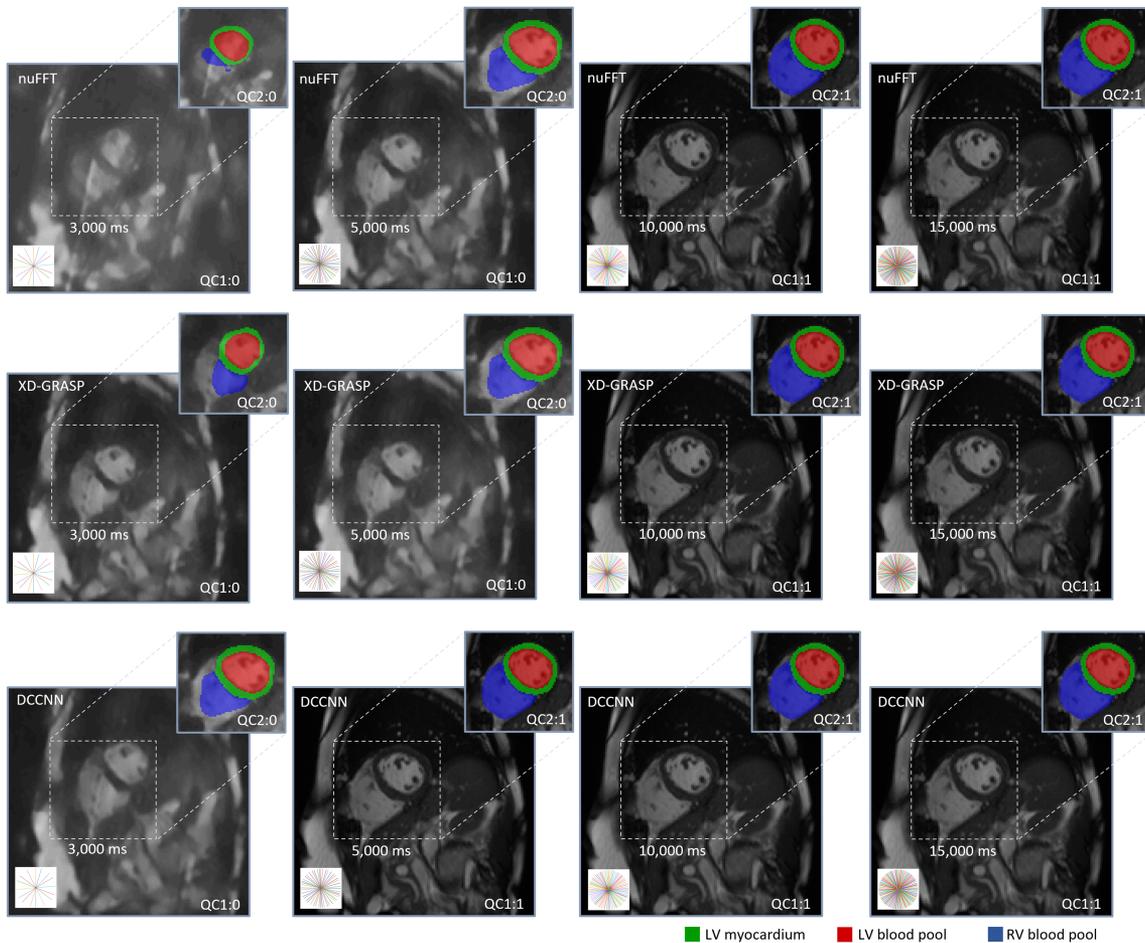
Fig. 5. Illustration of image reconstructions, segmentations and undersampling trajectories as a function of the scan time showing in each subplot using nuFFT (top row), XD-GRASP (middle row) and DCCNN (bottom row) using cine CMR complex images generated as sensitivity-weighted coil-combination. For this subject, we reconstructed cine CMR radially-acquired undersampled k-space data, with varying degrees of undersampling (scan times from 1000 ms to 15,000 ms), using the three reconstruction methods. The two QC steps were passed at a scan time of 10 seconds with the nuFFT, 6 seconds with the XD-GRASP and 4 seconds with the DCCNN, showing the ability of the framework to produce high-quality reconstructions and segmentations in a reduced scan time. QC = 1 means that the QC check was passed. nuFFT: non-uniform Fast Fourier Transform. XD-GRASP: Extra-dimensional golden-angle radial sparse parallel reconstruction. DCCNN: Deep Cascade of Convolutional Neural Networks. QC1: Image quality-control. QC2: Segmentation quality-control.

undersampling trajectories as a function of the scan time using nuFFT and DCCNN, and the output of each QC check for one healthy subject from Experiment II.

B. Segmentation Quality Analysis

Segmentation quality was quantified using the DSC between the GT segmentations from the fully-sampled image and segmentations that passed the QC check with the lowest scan time during simulated acquisition. Table II shows these results for Experiments I and II. We also present results for the three reconstruction methods and for healthy subjects and cardiomyopathy patients. Results are similar between healthy and cardiomyopathy patients and between the different reconstruction methods showing the ability of the QC checks to detect high-quality segmentations across different reconstruction algorithms and healthy/disease cases. The QC2 ResNet BACC, SEN and SPE on the testing set were equal to 88%, 82% and 94%, respectively, for the nuFFT, 87.3%, 81.5% and 94.3%, respectively, for the

XD-GRASP and 88.5%, 82% and 95%, respectively, for the DCCNN.

C. Functional Parameter Analysis

The performance of the proposed framework was evaluated using clinically relevant functional parameters: LVEDV, LVESV, LVEF, RVEDV, RVESV and RVEF, described in Section IV-E. A Bland-Altman analysis for the agreement between cardiac parameters estimated from fully-sampled data and via our DCCNN-based pipeline is shown in Fig. 6. To verify the significance of the biases, paired t-tests versus zero values were applied. The Pearson's correlation coefficients for Experiment I were equal to 0.98, 0.97 and 0.98 for LVEDV, LVESV and LVEF, respectively and 0.97, 0.95 and 0.96 for RVEDV, RVESV and RVEF, respectively. For Experiment II, the coefficients were equal to 0.97, 0.96 and 0.97 for LVEDV, LVESV and LVEF, respectively and 0.97, 0.95 and 0.96 for RVEDV, RVESV and RVEF, respectively. There was no significant difference in mean

TABLE II
DSC BETWEEN AUTOMATED AND MANUAL SEGMENTATIONS FOR EXPERIMENTS I AND II AFTER PASSING THE QC CHECKS FOR THE THREE
RECONSTRUCTION METHODS (NUFFT, XD-GRASP AND DCCNN)

		nuFFT		XD-GRASP		DCCNN	
		Healthy	Disease	Healthy	Disease	Healthy	Disease
Exp. I	LV	0.96 ± 0.06	0.95 ± 0.05	0.96 ± 0.05	0.95 ± 0.05	0.97 ± 0.04	0.96 ± 0.05
	RV	0.95 ± 0.06	0.94 ± 0.03	0.95 ± 0.05	0.95 ± 0.04	0.96 ± 0.05	0.95 ± 0.04
	MYO	0.91 ± 0.04	0.88 ± 0.07	0.92 ± 0.04	0.89 ± 0.04	0.93 ± 0.07	0.88 ± 0.08
Exp. II	LV	0.96 ± 0.04	N/A	0.96 ± 0.04	N/A	0.96 ± 0.05	N/A
	RV	0.94 ± 0.03	N/A	0.95 ± 0.06	N/A	0.94 ± 0.05	N/A
	MYO	0.91 ± 0.04	N/A	0.92 ± 0.05	N/A	0.92 ± 0.04	N/A

The mean and standard deviation are reported. In experiment II, all cases correspond to healthy subjects. LV: Left
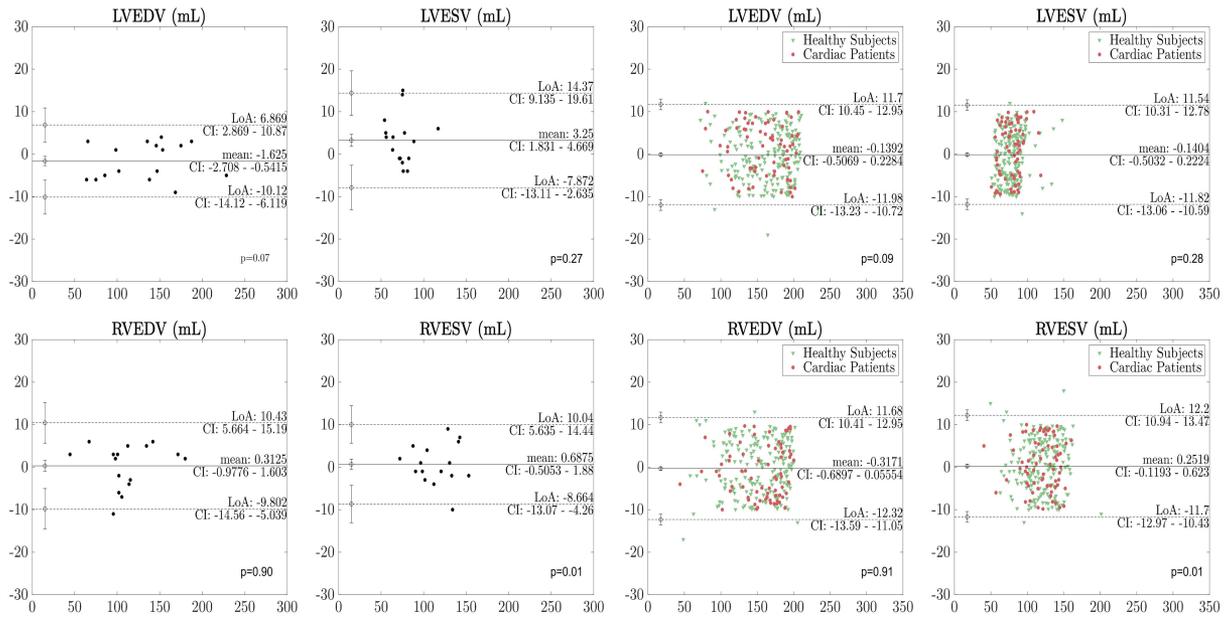ventricle. MYO: Myocardium. RV: Right ventricle.

Fig. 6. Bland-Altman plots for the agreement between cardiac parameters estimated from fully-sampled data and via our DCCNN-based pipeline
for Experiment I: 200 healthy subjects (in green) and 70 cardiomyopathy cases (in red) and Experiment II: cine CMR complex acquisitions of 16
healthy subjects (in black). The black solid line represents the mean bias and the black dotted lines the limits of agreement. The limits of agreement
are defined as the mean difference $\pm$ 1.96 SD of differences. The error bars represent the 95% confidence interval for both the upper and lower
limits of agreement. The p values represent the difference in mean bias from zero using a paired t-test.

absolute error between cardiac patients and healthy volunteers
for the output parameters.

Tables III and IV show the mean absolute difference and
mean relative difference across all subjects in clinical measures
between automated and GT segmentations for Experiment I
and Experiment II, respectively. Mean absolute and relative
differences are within the range of intra- and inter-observer
variability compared to [3]. Image quality is sufficient to allow
clinically relevant parameters to be automatically estimated to
within 5% mean absolute difference.

D. Scan Time

The proposed pipeline results in a reduced scan time for
2D+time cine CMR, which takes approximately 12 seconds in
our clinical protocol (spatial resolution $= 1.8 \times 1.8 \times 8.0$ mm^3,
temporal resolution $= 31.56$ ms and undersampling factor $=$
2). Table V shows the scan times at which the QC checks are
passed for Experiments I and II. By using a DCCNN for cine

CMR reconstruction, we pass QC checks after approximately 4
seconds of simulated acquisition, i.e. an undersampling factor of
4.5 with respect to the Cartesian fully-sampled data, compared to
approximately 12 seconds when using the nuFFT and 6 seconds
when using XD-GRASP. The DCCNN-based framework shows
scan time standard deviations of between 1 to 2 seconds (see
Table V), showing that the optimal undersampling factor varies
significantly on a scan-to-scan basis, confirming our hypothesis
outlined in Section I. Furthermore, when using the ground truth
binary quality labels, the mean and standard deviation of the opti-
mal scan time were equal to 4.03 and 1.21 seconds, respectively.

E. Qualitative Assessment

An experienced cardiologist visually assessed the predicted
segmentations for 55 test subjects. According to an in-house
standard operating procedure for image analysis and experi-
ence, the cardiologist visually compared automated segmen-
tation to manual segmentation and assessed whether the two

TABLE III
EXPERIMENT I: THE DIFFERENCE IN CLINICAL MEASURES BETWEEN AUTOMATED AND GT SEGMENTATIONS FOR A SET OF 200 HEALTHY SUBJECTS AND 70 CARDIOMYOPATHY (DISEASE) PATIENTS USING THREE RECONSTRUCTION METHODS: nuFFT, XD-GRASP AND DCCNN

		Healthy subjects		Cardiomyopathy patients	
		Absolute Difference	Relative Difference (%)	Absolute Difference	Relative Difference (%)
nuFFT	LVEDV (ml)	$4.53 \pm 2.01\ (0.00 - 5.32)$	$3.08 \pm 2.50\ (0.00 - 4.64)$	$5.06 \pm 2.88\ (0.07 - 5.32)$	$4.03 \pm 2.60\ (0.03 - 4.54)$
	LVESD (ml)	$4.16 \pm 2.94\ (0.00 - 6.12)$	$4.80 \pm 2.50\ (0.00 - 6.00)$	$3.03 \pm 2.96\ (0.01 - 3.40)$	$4.48 \pm 2.75\ (0.02 - 5.72)$
	LVEF (%)	$2.98 \pm 2.50\ (0.00 - 5.42)$	$4.59 \pm 2.98\ (0.01 - 5.68)$	$3.07 \pm 2.75\ (0.02 - 5.43)$	$4.98 \pm 2.57\ (0.03 - 5.24)$
	RVEDV (ml)	$6.01 \pm 2.98\ (0.23 - 7.24)$	$5.99 \pm 2.50\ (0.27 - 6.87)$	$3.67 \pm 4.52\ (0.13 - 4.50)$	$3.77 \pm 3.47\ (0.08 - 3.91)$
	RVESV (ml)	$3.72 \pm 3.23\ (0.16 - 4.45)$	$3.18 \pm 3.51\ (0.28 - 4.54)$	$3.90 \pm 3.63\ (0.14 - 4.75)$	$3.96 \pm 2.96\ (0.23 - 4.70)$
	RVEF (%)	$3.64 \pm 2.38\ (0.00 - 5.93)$	$7.03 \pm 4.48\ (0.00 - 8.19)$	$4.55 \pm 3.33\ (0.00 - 4.88)$	$5.91 \pm 3.86\ (0.01 - 6.34)$
XD-GRASP	LVEDV (ml)	$2.81 \pm 2.72\ (0.17 - 5.28)$	$2.44 \pm 2.12\ (0.16 - 6.27)$	$3.75 \pm 2.53\ (0.05 - 3.98)$	$4.56 \pm 2.18\ (0.04 - 4.74)$
	LVESD (ml)	$3.88 \pm 2.67\ (0.07 - 6.35)$	$3.56 \pm 4.71\ (0.10 - 7.15)$	$2.23 \pm 2.64\ (0.03 - 3.41)$	$3.32 \pm 2.95\ (0.04 - 4.88)$
	LVEF (%)	$2.67 \pm 2.08\ (0.04 - 5.74)$	$2.86 \pm 3.33\ (0.03 - 6.51)$	$2.95 \pm 2.82\ (0.05 - 3.42)$	$3.52 \pm 2.23\ (0.08 - 4.74)$
	RVEDV (ml)	$4.98 \pm 2.51\ (0.02 - 5.14)$	$4.67 \pm 3.40\ (0.02 - 6.44)$	$4.10 \pm 2.21\ (1.82 - 4.54)$	$3.16 \pm 2.41\ (1.42 - 3.99)$
	RVESV (ml)	$2.07 \pm 3.73\ (0.05 - 2.84)$	$4.33 \pm 3.11\ (0.07 - 5.29)$	$3.09 \pm 2.41\ (0.05 - 3.46)$	$2.92 \pm 3.07\ (0.06 - 3.23)$
	RVEF (%)	$2.98 \pm 4.32\ (0.03 - 3.32)$	$4.10 \pm 2.11\ (0.03 - 4.95)$	$3.12 \pm 2.18\ (0.04 - 3.94)$	$3.32 \pm 3.50\ (0.03 - 4.97)$
DCCNN	LVEDV (ml)	$2.78 \pm 2.50\ (0.16 - 5.35)$	$2.03 \pm 2.07\ (0.13 - 6.14)$	$3.62 \pm 2.48\ (0.03 - 3.96)$	$4.45 \pm 2.07\ (0.02 - 4.49)$
	LVESD (ml)	$3.05 \pm 2.32\ (0.05 - 6.08)$	$3.25 \pm 4.69\ (0.09 - 7.00)$	$2.19 \pm 2.51\ (0.02 - 3.08)$	$3.19 \pm 2.72\ (0.02 - 4.87)$
	LVEF (%)	$2.47 \pm 2.06\ (0.01 - 5.67)$	$2.78 \pm 3.25\ (0.01 - 6.49)$	$2.91 \pm 2.61\ (0.04 - 3.42)$	$3.47 \pm 2.19\ (0.07 - 4.66)$
	RVEDV (ml)	$4.98 \pm 2.40\ (0.01 - 5.03)$	$4.35 \pm 3.33\ (0.01 - 6.42)$	$4.01 \pm 2.20\ (1.78 - 4.33)$	$3.06 \pm 2.21\ (1.41 - 3.64)$
	RVESV (ml)	$2.04 \pm 3.61\ (0.05 - 2.76)$	$4.28 \pm 3.09\ (0.07 - 5.08)$	$3.07 \pm 2.92\ (0.04 - 3.23)$	$2.89 \pm 3.00\ (0.05 - 3.12)$
	RVEF (%)	$2.85 \pm 4.20\ (0.00 - 3.11)$	$4.08 \pm 2.01\ (0.01 - 4.82)$	$3.06 \pm 2.17\ (0.00 - 3.87)$	$3.17 \pm 3.53\ (0.01 - 4.93)$

The minimum and maximum (in parenthesis), mean and standard deviation of the absolute and relative differences for the six cardiac functional parameters (LV and RV EDV, ESV and EF) are reported.

TABLE IV
EXPERIMENT II: THE DIFFERENCE IN CLINICAL MEASURES BETWEEN AUTOMATED AND GT SEGMENTATIONS FOR A SET OF 16 CASES USING DCCNN

	Absolute Difference	Relative Difference (%)
LVEDV (ml)	$2.98 \pm 2.38\ (0.00 - 4.24)$	$3.04 \pm 3.76\ (0.00 - 4.98)$
LVESD (ml)	$3.98 \pm 2.55\ (0.01 - 4.59)$	$4.30 \pm 2.50\ (0.02 - 5.42)$
LVEF (%)	$3.01 \pm 2.50\ (0.01 - 4.42)$	$3.58 \pm 2.98\ (0.01 - 4.68)$
RVEDV (ml)	$3.72 \pm 3.97\ (0.23 - 5.24)$	$3.00 \pm 2.50\ (0.27 - 4.87)$
RVESV (ml)	$4.01 \pm 3.23\ (0.15 - 6.45)$	$5.18 \pm 4.51\ (0.28 - 5.43)$
RVEF (%)	$3.84 \pm 2.38\ (0.01 - 5.93)$	$4.89 \pm 3.90\ (0.01 - 5.10)$

The minimum and maximum (in parenthesis), mean and standard deviation of the absolute and relative differences for the six cardiac functional parameters (LV and RV EDV, ESV and EF) are reported.

segmentations achieved a good agreement or not. The visual assessment was performed for basal, mid-ventricular and apical slices. For mid-ventricular slices, automated segmentation was found to agree well with manual segmentation for 92.7% of the cases by visual inspection. For basal and apical slices where the ventricular contours are more complex and thus more difficult to segment, automated segmentation was found to agree well with manual segmentation for 72.7% and 81.8% of the cases, respectively.

VII. DISCUSSION AND CONCLUSION

This work demonstrates the feasibility of a DL-based framework for automated quality-controlled reconstruction and analysis of undersampled cine SAX CMR data without a previously defined level of undersampling. This framework has the potential to jointly accelerate time-consuming cine image acquisition and cumbersome manual image analysis achieving performance comparable to human experts in fully-sampled data. Our results show that we can produce quality-controlled images and segmentations, as shown in Tables I and II, respectively, in a scan time reduced from 12 to 4 seconds per slice, as shown in Table V, enabling reliable estimates of cardiac functional parameters within 5% mean absolute error, as shown in Tables III and IV, and Fig. 6. The results demonstrate that the optimal undersampling factor varies for different subjects from

1 to 2 seconds per slice and that our framework can adapt to these differences. The reconstruction for each image frame took approximately 30 ms. Furthermore, on a GPU, the inference time for each network in the downstream analysis was approximately 23 ms per cardiac frame. This circumvents costly image reconstructions, enabling fast post-processing immediately following accelerated and, thus, fast cine acquisitions. These times mean that real-time application of the framework on the MR scanner is feasible. Our ultimate aim is to develop an active acquisition scheme in which acquisition can be stopped as soon as acquired data are sufficient to produce high-quality reconstructions and segmentations. In this article, we performed a proof-of-concept using retrospective undersampled data. To achieve true active acquisition, alterations to the software of the scanner would have to be made, such that a signal is sent to the acquisition when all needed data have been acquired.

The incorporation of robust QC steps ensures that the outputs of the framework (images, segmentations and functional metrics) are all of diagnostic quality and errors are within the range of inter-observer variability. In an automated image analysis pipeline, this method would deliver high-quality performance at high speeds and at a large scale. The framework could also provide real-time feedback during image acquisition, indicating if an acquired image is of sufficient quality for the downstream analysis tasks.

Even though our model achieved high performance levels, one limitation is that the cine CMR dataset featuring real phase is still relatively small (16 subjects), and all datasets were acquired at a single site on a single scanner. Therefore further work needs to be done to ensure the generalization ability of the framework. Future research will need to explore more generalizable methods for analysing a wider range of CMR images, such as multi-site images acquired from different machines, different imaging protocols and integration of automated segmentation results into diagnostic reports. Nevertheless, this work represents an important proof-of-concept for the potential of integrated frameworks for reconstruction and downstream analysis. In conclusion, we believe that the proposed approach could have great clinical

	nuFFT		XD-GRASP		DCCNN	
	Healthy	Disease	Healthy	Disease	Healthy	Disease
Experiment I	12.43 ± 1.62	12.85 ± 2.03	5.91 ± 1.89	6.32 ± 2.02	4.08 ± 1.35	4.02 ± 2.23
Experiment II	12.89 ± 1.81	N/A	5.82 ± 1.73	N/A	4.01 ± 1.12	N/A

The mean and standard deviation are reported. In experiment II, all cases correspond to healthy subjects.

utility, reducing redundancies in the CMR acquisition process whilst still providing high-quality diagnostic images and robust estimates of functional parameters.

ACKNOWLEDGMENT

REFERENCES

[1] J. Schlemper et al., "A deep cascade of convolutional neural networks for dynamic MR image reconstruction," *IEEE Trans. Med. Imag.*, vol. 37, no. 2, pp. 491–503, Feb. 2018.

[2] K. Hammernik et al., "Learning a variational network for reconstruction of accelerated MRI data," *Magn. Reson. Med.*, vol. 79, no. 6, pp. 3055–3071, 2018.

[3] W. Bai et al., "Automated cardiovascular magnetic resonance image analysis with fully convolutional networks," *J. Cardiovasc. Magn. Reson.*, vol. 20, no. 1, 2018, Art. no. 65.

[4] B. Ruijsink et al., "Fully automated, quality-controlled cardiac analysis from CMR: validation and large-scale application to characterize cardiac function," *Cardiovasc. Imag.*, vol. 13, no. 3, pp. 684–695, 2020.

[5] J. Schlemper et al., "Cardiac MR segmentation from undersampled K-space using deep latent representation learning," in *Proc. Int. Conf. Med. Image Comput. Comput.- Assist. Intervention*, 2018, pp. 259–267.

[6] I. Oksuz et al., "High-quality segmentation of low quality cardiac MR images using K-space artefact correction," in *Proc. Medical Imag. Deep Learn. Conf.*, PMLR, 2019, pp. 380–389.

[7] I. Oksuz et al., "Deep learning-based detection and correction of cardiac MR motion artefacts during reconstruction for high-quality segmentation," *IEEE Trans. Med. Imag.*, vol. 39, no. 12, pp. 4001–4010, Dec. 2020.

[8] M. Uecker et al., "ESPIRiT – an eigenvalue approach to autocalibrating parallel MRI: where SENSE meets GRAPPA," *Magn. Reson. Med.*, vol. 71, no. 3, pp. 990–1001, 2014.

[9] R.-M. Menchn-Lara et al., "Reconstruction techniques for cardiac cine MRI," *Insights Imag.*, vol. 10, no. 1, pp. 1–16, 2019.

[10] T. Küstner et al., "CINENet: Deep learning-based 3D cardiac CINE MRI reconstruction with multi-coil complex-valued 4D spatio-temporal convolutions," *Sci. Rep.*, vol. 10, no. 1, pp. 1–13, 2020.

[11] C. Qin et al., "Convolutional recurrent neural networks for dynamic MR image reconstruction," *IEEE Trans. Med. Imag.*, vol. 38, no. 1, pp. 280–290, Jan. 2019.

[12] W. Shi et al., "Real-time single image and video super-resolution using an efficient sub-pixel convolutional neural network," in *Proc. IEEE Conf. Comput. Vis. Pattern Recognit.*, 2016, pp. 1874–1883.

[13] B. Zhu et al., "Image reconstruction by domain-transform manifold learning," *Nature*, vol. 555, no. 7697, pp. 487–492, 2018.

[14] D. Lee et al., "Deep residual learning for accelerated MRI using magnitude and phase networks," *IEEE Trans. Biomed. Eng.*, vol. 65, no. 9, pp. 1985–1995, Sep. 2018.

[15] P. Peng et al., "A review of heart chamber segmentation for structural and functional analysis using cardiac magnetic resonance imaging" *Magn. Reson. Mater. Phys., Biol. Med.*, vol. 29, no. 2, pp. 155–195, 2016.

[16] O. Ronneberger, P. Fischer, and T. Brox, "U-Net: Convolutional networks for biomedical image segmentation," in *Proc. Int. Conf. Med. Image Comput. Comput.- Assist. Intervention*, 2015, pp. 234–241.

[17] L. V. Romaguera et al., "Myocardial segmentation in cardiac magnetic resonance images using fully convolutional neural networks," *Biomed. Signal Process. Control*, vol. 44, pp. 48–57, 2018.

[18] F. Isensee et al., "nnU-Net: A self-configuring method for deep learning-based biomedical image segmentation," *Nature Methods*, vol. 18, no. 2, pp. 203–211, 2021.

[19] J. M. Harana et al., "Large-scale, multi-vendor, multi-protocol, quality-controlled analysis of clinical cine CMR using artificial intelligence," *Eur. Heart J. - Cardiovasc. Imag.*, vol. 22, no. Supplement_2, 2021, Art. no. jeab090.046.

[20] O. Bernard et al., "Deep learning techniques for automatic MRI cardiac multi-structures segmentation and diagnosis: Is the problem solved?" *IEEE Trans. Med. Imag.*, vol. 37, no. 11, pp. 2514–2525, Nov. 2018.

[21] R. Attar et al., "Quantitative CMR population imaging on 20,000 subjects of the UK Biobank imaging study: LV/RV quantification pipeline and its evaluation," *Med. Image Anal.*, vol. 56, pp. 26–42, 2019.

[22] W. Bai et al., "A population-based phenome-wide association study of cardiac and aortic structure and function," *Nature Med.*, vol. 26, no. 10, pp. 1654–1662, 2020.

[23] H. Mojibian and H. Pouraliakbar, "Cardiac magnetic resonance imaging" in *Practical Cardiology*. Amsterdam, The Netherlands: Elsevier, 2022, pp. 175–183.

[24] T. Küstner et al., "A machine-learning framework for automatic reference-free quality assessment in MRI," *Magn. Reson. Imag.*, vol. 53, pp. 134–147, 2018.

[25] L. Zhang et al., "Automated quality assessment of cardiac MR images using convolutional neural networks" in *Proc. Int. Workshop Simul. Synth. Med. Imag.*, 2016, pp. 138–145.

[26] I. Oksuz et al., "Automatic CNN-based detection of cardiac MR motion artefacts using K-space data augmentation and curriculum learning," *Med. Image Anal.*, vol. 55, pp. 136–147, 2019.

[27] R. Robinson et al., "Automated quality control in image segmentation: Application to the UK Biobank cardiovascular magnetic resonance imaging study," *J. Cardiovasc. Magn. Reson.*, vol. 21, no. 1, pp. 1–14, 2019.

[28] F. Galati and M. A. Zuluaga, "Efficient model monitoring for quality control in cardiac image segmentation," in *Proc. Int. Conf. Funct. Imag. Model. Heart*, 2021, pp. 101–111.

[29] J. Fournel et al., "Medical image segmentation automatic quality control: A multi-dimensional approach," *Med. Image Anal.*, vol. 74, 2021, Art. no. 102213.

[30] I. Machado et al., "Quality-aware cine cardiac MRI reconstruction and analysis from undersampled K-space data," in *Proc. Int. Workshop Stat. Atlases Comput. Models Heart*, 2021, pp. 12–20.

[31] S. E. Petersen et al., "UK Biobank's cardiovascular magnetic resonance protocol," *J. Cardiovasc. Magn. Reson.*, vol. 18, no. 1, 2015, Art. no. 8.

[32] F. Knoll et al., "GPUNUFFT-an open source GPU library for 3D regridding with direct Matlab interface," in *Proc. 22nd Annu. Meeting ISMRM*, 2014, vol. 4297. [Online]. Available: https://scholar.google.com/scholar?hl=en&as_sdt=0%2C5&q=gpuNUFFT+-+An+Open+Source+GPU+Library+for+3D+Regridding+with+Direct+Matlab+Interface&btnG=

[33] K. He et al., "Deep residual learning for image recognition," in *Proc. IEEE Conf. Comput. Vis. Pattern Recognit.*, 2016, pp. 770–778.

[34] C. Chen et al., "Improving the generalizability of convolutional neural network-based segmentation on CMR images," *Front. Cardiovasc. Med.*, vol. 7, 2020, Art. no. 105.

[35] J. P. Haldar, "Low-rank modeling of local k-space neighborhoods (LORAKS) for constrained MRI," *IEEE Trans. Med. Imag.*, vol. 33, no. 3, pp. 668–681, Mar. 2014.

[36] S. Winkelmann et al., "An optimal radial profile order based on the Golden Ratio for time-resolved MRI," *IEEE Trans. Med. Imag.*, vol. 26, no. 1, pp. 68–76, Jan. 2007.

[37] J. A. Fessler, "On NUFFT-based gridding for non-cartesian MRI," *J. Magn. Reson.*, vol. 188, no. 2, pp. 191–195, 2007.

[38] L. Feng et al., "XD-GRASP: Golden-angle radial MRI with reconstruction of extra motion-state dimensions using compressed sensing," *Magn. Reson. Med.*, vol. 75, no. 2, pp. 775–788, 2016.